Catalysis Today 147 (2009) 68–76

Contents lists available at ScienceDirect

Catalysis Today

journal homepage: www.elsevier.com/locate/cattod

CO_2 adsorption and activation over γ-Al_2O_3-supported transition metal dimers: A density functional study

Yun-xiang Pan [a,b], Chang-jun Liu [a], Tomasz S. Wiltowski [c], Qingfeng Ge [b,*]

[a] Key Laboratory for Green Chemical Technology of Ministry of Education, School of Chemical Engineering, Tianjin University, Tianjin 300072, China
[b] Department of Chemistry and Biochemistry, Southern Illinois University, 1245 Lincoln Drive, Carbondale, IL 62901, USA
[c] Department of Mechanical Engineering and Energy Processes and Coal Research Center, Southern Illinois University, Carbondale, IL 62901, USA

ARTICLE INFO

Article history:
Available online 10 June 2009

Keywords:
CO_2 adsorption and activation
Transition metal dimers
γ-Al_2O_3
Density functional theory

ABSTRACT

Catalytic conversion of CO_2 to liquid fuels has the benefit of reducing CO_2 emission. Adsorption and activation of CO_2 on the catalyst surface are key steps of the conversion. Herein, we used density functional theory (DFT) slab calculations to study CO_2 adsorption and activation over the γ-Al_2O_3-supported 3d transition metal dimers (M_2/γ-Al_2O_3, M = Sc–Cu). CO_2 was found to adsorb on M_2/γ-Al_2O_3 negatively charged and in a bent configuration, indicating partial activation of CO_2. Our results showed that both the metal dimer and the γ-Al_2O_3 support contribute to the activation of the adsorbed CO_2. The presence of a metal dimer enhances the interaction of CO_2 with the substrate. Consequently, the adsorption energy of CO_2 on M_2/γ-Al_2O_3 is significantly higher than that on the γ-Al_2O_3 surface without the metal dimer. The decreasing binding strength of CO_2 on M_2/γ-Al_2O_3 as M_2 changes from Sc_2 to Cu_2 was attributed to decreasing electron-donation by the supported metal dimers. Hydroxylation of the support surface reduces the amount of charge transferred to CO_2 for the same metal dimer and weakens the CO_2 chemisorption bonds. Highly dispersed metal particles maintained at a small size are expected to exhibit good activity toward CO_2 adsorption and activation.

1. Introduction

Catalytic conversion of carbon dioxide (CO_2) into liquid fuels has been identified as one of the priority research directions in a recent U.S. Department of Energy Report, "Basic Research Needs: Catalysis for Energy" [1]. Recycling CO_2 to make liquid fuels neutralizes CO_2 emissions, thereby alleviating the greenhouse effect caused by CO_2. However, converting CO_2 to liquid fuel is an energy-intensive process due to the nature of the reactions involved. Carbon dioxide can be used as a reforming reagent for methane to produce synthesis gas ($CO + H_2$) [2–11], which can then be converted to liquid fuels. Fe-, Co- and Ni-based catalysts were found to have reasonable activities for CO_2 reforming of methane [4–11]. Alternatively, CO_2 can be directly hydrogenated, where the products from direct CO_2 hydrogenation depend on the catalysts used. Over the Ni-based catalysts, methane is one of the main products [12–14]. On the other hand, methanol will be produced predominantly over the Cu-based catalysts [15,16]. In these heterogeneous CO_2 conversion processes, adsorption of CO_2 and activation of the C–O bond are key steps. A detailed characterization of CO_2 interaction with the catalysts at the molecular level will help us to better understand the underlying mechanisms of the reactions and aid in the elucidation of key factors that affect the performance of the catalysts.

There have been many studies on the interaction between CO_2 and transition metal surfaces [17]. On the basis of combined experimental and computational studies, Vesselli et al. [18] suggested that the CO_2 molecule was adsorbed on the Ni (1 1 0) surface through the carbon atom in a negatively charged and bent configuration. Wang et al. studied the chemisorption of CO_2 on the Ni (1 1 1), Ni (1 0 0) and Ni (1 1 0) surfaces using DFT methods and reported that the C=O bond of CO_2 was activated due to electron transfer from the Ni surface into the anti-bonding orbital of CO_2 [19]. The C=O bond activation ability of the Ni surfaces was suggested to be in the order of Ni (1 1 0) > Ni (1 0 0) > Ni (1 1 1). UV photoelectron spectroscopy, X-ray photoelectron spectroscopy and Auger electron spectroscopy have all been applied to characterize CO_2 adsorption on potassium-covered Fe (1 1 0) surface at 85 K [20,21]. A small amount of CO_2 was found to dissociate into CO and oxygen whereas the molecularly adsorbed CO_2 was found in a bent configuration.

The mechanisms for CO_2 adsorption and activation over the oxide-supported metal catalysts are expected to be different from that on the pure metal surfaces due to the presence of the oxide support. Aksoylu and Önsan [14] investigated CO_2 adsorption and methanation over oxide-supported nickel catalysts. They found

* Corresponding author. Tel.: +1 618 453 6406; fax: +1 618 453 6408.
E-mail address: qge@chem.siu.edu (Q. Ge).

0920-5861/$ – see front matter © 2009 Elsevier B.V. All rights reserved.
doi:10.1016/j.cattod.2009.05.005

that the oxide support has no activity for methanation but is active for CO_2 adsorption and activation. de Leitenburg et al. [22] studied the interaction between CO_2 and the ceria-supported late transition metals (Rh, Ru, Pt, Pd and Ir). They reported that CO_2 activation on the surface Ce^{3+} sites led to the formation of CO, followed by the oxidation of Ce^{3+} to Ce^{4+}. The presence of oxygen vacancies in ceria created additional reduction potential for the reduction of CO_2 to CO and/or surface carbonaceous species. The carbonaceous species were rapidly hydrogenated to CH_4 over the supported metals. The effect of the support on CO_2 adsorption and activation was also reported over the oxide-supported Rh catalysts. On a clean Rh surface the adsorption of CO_2 is weak and non-dissociative, whereas over the oxide-supported Rh catalysts CO_2 dissociates easily [23,24].

Alumina, γ-Al_2O_3 in particular, has been commonly used as support in heterogeneous catalysis, including CO_2 conversion. However, a detailed characterization of the γ-Al_2O_3-supported metal catalysts as well as their activity toward CO_2 adsorption and activation is not readily available. This can be partly attributed to the structural complexity of γ-Al_2O_3 [25–28]. The γ-Al_2O_3 structural models based on the defective spinel model [25,29] and non-spinel model [27] have been proposed. We employed both types of models in our previous studies [30–33]. In the present study, we chose the non-spinel model based on the fact that its (1 0 0) surface exposes the penta-Al sites that were observed experimentally [34,35]. Herein, we used density functional theory (DFT) slab calculations to study the interaction of CO_2 with the γ-Al_2O_3-supported 3d transition metal dimers (Sc_2, Ti_2, V_2, Cr_2, Mn_2, Fe_2, Co_2, Ni_2 and Cu_2). The dimers were used since they are the smallest units that allow us to probe both metal–metal and metal–support interactions. In fact, features of dimer have been directly imaged on γ-Al_2O_3 [36]. We selected the (1 1 0) surface of γ-Al_2O_3 to model the support for the transition metal dimers. This is based on the fact that the (1 1 0) surface was estimated to account for 83% of the total surface area of γ-Al_2O_3 and is expected to dominate the exposed surfaces on γ-Al_2O_3 nanocrystallites [27].

This paper is organized as follows. Computational method and models are described in Section 2. Results and discussion are given in Section 3. Finally, the main conclusions are presented in Section 4. For clarity of presentation, the transition metal dimers will be referred to as M_2 with M = Sc–Cu in the following discussions when a distinction of the metal is not necessary.

2. Computational methodology and models

The methodology and the γ-Al_2O_3 model are similar to those used in our previous studies [30,33]. All the calculations were performed by using the Vienna ab-initio simulation package (VASP) [37]. The projector augmented wave method was used to describe the interaction between ions and electrons [38,39] and the PAW potentials of the 3d elements have been used our previous calculations [40]. The non-local exchange-correlation energy was evaluated using the Perdew–Burke–Ernzehof functional [41]. A plane wave basis set with a cutoff energy of 400 eV was used. A $(2 \times 2 \times 1)$ grid was used to generate *k*-points according to the Monkhorst–Pack method [42]. Test calculations with a *k*-point grid of $(4 \times 4 \times 1)$ gave a numerical difference in CO_2 adsorption energy of less than 0.005 eV. The atomic structures were relaxed using the conjugate gradient algorithm scheme as implemented in the VASP code until the forces on unconstrained atoms were <0.03 eV/Å. Bader charge analyses were also performed for all the adsorption systems [43,44].

The unit cell size of the γ-Al_2O_3 (1 1 0) surface and the number of the Al_2O_3 layers were kept the same as in our previous study [33]. The γ-Al_2O_3 (1 1 0) surface was modeled by a supercell with a dimension of (8.40 Å × 8.07 Å × 19.18 Å). Twelve Al_2O_3 molecular units in the slab were distributed in six layers. The vacuum region separating the slabs along [0 0 1] direction was set to 12 Å. In all calculations, the bottom two layers were frozen in their bulk positions, whereas the remaining four layers together with M_2, the adsorbed CO_2 and/or hydroxyls were allowed to relax.

The binding energy of M_2 with the surface, $\Delta E_{binding}$, was calculated as follows:

$$\Delta E_{binding} = -(E_{M_2/\gamma\text{-}Al_2O_3} - E_{\gamma\text{-}Al_2O_3} - E_{M_2})$$

where $E_{M_2/\gamma\text{-}Al_2O_3}$, $E_{\gamma\text{-}Al_2O_3}$ and E_{M_2} are the total energies of γ-Al_2O_3 slab with M_2, the bare γ-Al_2O_3 slab and the free M_2, respectively. The adsorption energy of CO_2, ΔE_{ad}, was defined as:

$$\Delta E_{ad} = -(E_{CO_2-M_2/\gamma\text{-}Al_2O_3} - E_{M_2/\gamma\text{-}Al_2O_3} - E_{CO_2})$$

where $E_{CO_2-M_2/\gamma\text{-}Al_2O_3}$ and E_{CO_2} represent the total energies of the slab simulating CO_2 adsorbed on M_2/γ-Al_2O_3 and the free CO_2 molecule, respectively. The energy of the free CO_2 molecule, E_{CO_2}, was computed by placing a single CO_2 molecule in a 10 Å × 10 Å × 10 Å cubic box. Consequently, positive values of $\Delta E_{binding}$ or ΔE_{ad} indicate energetically favorable processes according to these definitions of binding energy and adsorption energy.

3. Results and discussion

3.1. M_2 supported on the dry γ-Al_2O_3 (1 1 0) surface

The top view of the dry γ-Al_2O_3 (1 1 0) surface was provided in Fig. 1a to label the surface atoms. On the dry surface, 3-fold-coordinated aluminum (Al_{3c}), 4-fold-coordinated aluminum (Al_{4c}), 2-fold-coordinated oxygen (O_{2c}) and 3-fold-coordinated oxygen

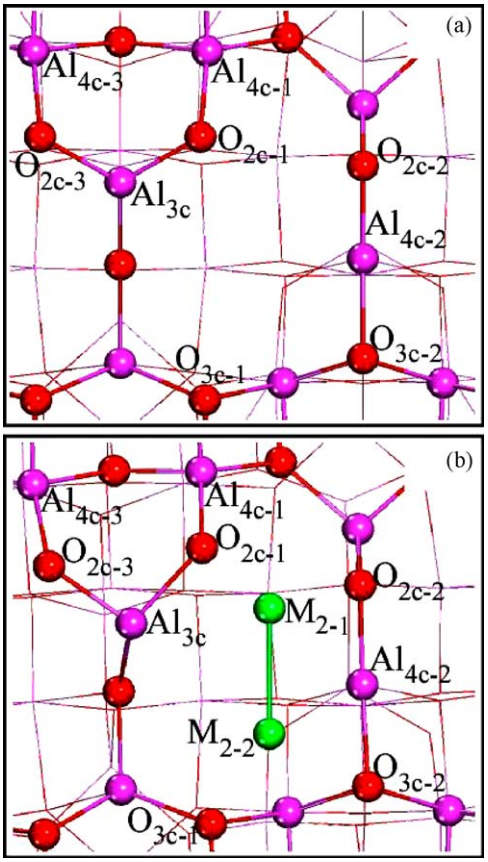

Fig. 1. Top view of the dry γ-Al_2O_3 (1 1 0) surface (a) and the schematic structural model of D(M_2) (b). Color coding: red, O atoms; pink, Al atoms; green, M atoms. (For interpretation of the references to color in this figure legend, the reader is referred to the web version of the article.)

(O_{3c}) atoms are exposed, among which Al_{3c}, Al_{4c} and O_{2c} are coordinately unsaturated. When adsorption involves more than one atom of the same type of surface sites, the sites will be distinguished by adding an additional subscript. For example, Sc_1–$O_{2c\text{-}2}$ represents the bond formed between the first Sc atom in the Sc dimer and the second O_{2c} atom at the binding site. Different surface sites were explored for M_2 adsorption, and adsorption at these sites resulted in a number of configurations. The most stable adsorption configuration of M_2 among the stable sites was selected as the substrate in the study of CO_2 adsorption and was named as $D(M_2)$, with D indicating the dry oxide surface. For example, $D(Ni_2)$ represents the most stable configuration for Ni_2 supported on the dry surface. A schematic structural model of $D(M_2)$ is shown in Fig. 1b. In $D(M_2)$, the dimer is located at a site surrounded by two O_{2c} atoms ($O_{2c\text{-}1}$ and $O_{2c\text{-}2}$), two O_{3c} atoms ($O_{3c\text{-}1}$ and $O_{3c\text{-}2}$), an Al_{3c} atom and an Al_{4c} ($Al_{4c\text{-}2}$) atom. We kept the two metal atoms in dimer form and did not explore the configuration in which metal atoms are separated from each other. The binding energies of M_2 in $D(M_2)$ as well as the distances between metal and surface atoms are summarized in Table 1.

Among all M_2 from Sc_2 to Cu_2, Sc_2 exhibits the strongest binding with the dry surface, with a binding energy of 4.65 eV. In $D(Sc_2)$, the distances between Sc and the surface O atoms, $Sc_{2\text{-}1}$–$O_{2c\text{-}1}$, 2.00 Å, $Sc_{2\text{-}1}$–$O_{2c\text{-}2}$, 2.01 Å, $Sc_{2\text{-}2}$–$O_{3c\text{-}1}$, 2.11 Å and $Sc_{2\text{-}2}$–$O_{3c\text{-}2}$, 2.06 Å, indicate that bonds were formed between the atom pairs. The binding energy of Ti_2 in $D(Ti_2)$ is 4.19 eV, which is lower by 0.46 eV than that of Sc_2 in $D(Sc_2)$. In $D(Ti_2)$, the $Ti_{2\text{-}1}$ atom bonds to the surface $O_{2c\text{-}1}$ and $O_{2c\text{-}2}$ atoms whereas the $Ti_{2\text{-}2}$ atom bonds to the surface $O_{3c\text{-}1}$ atom only. The bond distances of $Ti_{2\text{-}1}$–$O_{2c\text{-}1}$, $Ti_{2\text{-}1}$–$O_{2c\text{-}2}$ and $Ti_{2\text{-}2}$–$O_{3c\text{-}1}$ are 1.95 Å, 1.96 Å, and 2.20 Å, respectively. As we moved to V_2, the binding energy decreases significantly, as shown in Table 1. In $D(V_2)$, V_2 appears to bound with one end of the dimer ($V_{2\text{-}1}$–$O_{2c\text{-}1}$ and $V_{2\text{-}1}$–$O_{2c\text{-}2}$). Among all M_2, Cr_2 shows the weakest binding with the surface, with a binding energy of 2.07 eV, although both ends of Cr_2 interact with the surface, as indicated by the distances: $Cr_{2\text{-}1}$–$O_{2c\text{-}1}$ (1.97 Å), $Cr_{2\text{-}1}$–$O_{2c\text{-}2}$ (1.97 Å), $Cr_{2\text{-}2}$–$O_{3c\text{-}1}$ (2.09 Å) and $Cr_{2\text{-}2}$–$O_{3c\text{-}2}$ (2.07 Å). As shown in Table 1, the binding energy of Mn_2 in $D(Mn_2)$ is higher by 0.95 eV than that of Cr_2 in $D(Cr_2)$. In $D(Mn_2)$, $Mn_{2\text{-}1}$–$O_{2c\text{-}1}$ (1.97 Å), $Mn_{2\text{-}1}$–$O_{2c\text{-}2}$ (1.99 Å) and $Mn_{2\text{-}2}$–$O_{3c\text{-}1}$ (2.04 Å) bonds were formed between Mn_2 and the surface. From Mn_2 to Cu_2, the binding energy only increases slightly, from 3.02 eV to 3.33 eV. $D(Fe_2)$, $D(Co_2)$, $D(Ni_2)$ and $D(Cu_2)$ have similar structures in which M_2 interacts with the surface through $M_{2\text{-}1}$–$O_{2c\text{-}1}$, $M_{2\text{-}1}$–$O_{2c\text{-}2}$ and $M_{2\text{-}2}$–$O_{3c\text{-}1}$ bonds. For example, the three bonds in $D(Ni_2)$ are $Ni_{2\text{-}1}$–$O_{2c\text{-}1}$ (1.91 Å), $Ni_{2\text{-}1}$–$O_{2c\text{-}2}$ (2.09 Å) and $Ni_{2\text{-}2}$–$O_{3c\text{-}1}$ (2.05 Å).

3.2. CO_2 adsorption and activation on $D(M_2)$

Different CO_2 adsorption configurations on $D(M_2)$ were explored and three adsorption configurations η_1, η_2 and η_3 were found to be stable. In this section, the structural properties of these adsorption configurations will be described first. For clarity, the oxygen atoms of CO_2 were labeled as O_a and O_b if the two atoms were located at unequivalent positions.

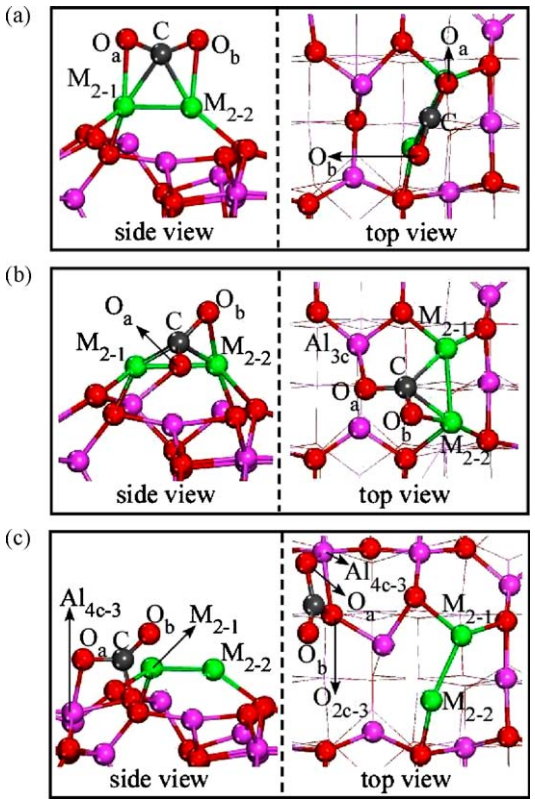

Fig. 2. Schematic structural models of adsorption configurations η_1 (a), η_2 (b) and η_3 (c). Color coding, grey, C atoms; others are the same as in Fig. 1.

A schematic structural model for η_1 configuration is shown in Fig. 2a. In η_1, CO_2 interacts with $D(M_2)$ through C–$M_{2\text{-}1}$, C–$M_{2\text{-}2}$, O_a–$M_{2\text{-}1}$ and O_b–$M_{2\text{-}2}$ bonds. The adsorbed CO_2 is in a geometry that was greatly distorted from the free CO_2 molecule. In Fig. 3, the variations of the C–O_a and C–O_b bond distances and the O_a–C–O_b angle were plotted against the metals. The structural parameters of the free CO_2 molecule and CO_3^{2-} ion were also plotted in the figure for references. Both the C–O_a and C–O_b bonds were elongated from the C–O bond in free CO_2 and the O_a–C–O_b angle was reduced significantly in η_1 from 180°. For instance, in the η_1 configuration on $D(Ni_2)$, the C–O_a and C–O_b bonds are 1.27 Å and 1.28 Å, respectively, and the O_a–C–O_b angle is 138°. Elongation of the C–O bonds and reduction of the O–C–O angle indicate the partial activation of CO_2 [19]. The variation of the $M_{2\text{-}1}$–$M_{2\text{-}2}$ bond distance before and after CO_2 adsorption is also shown in Fig. 3d. Clearly, the adsorption of CO_2 in η_1 configuration on $D(M_2)$ made the $M_{2\text{-}1}$–$M_{2\text{-}2}$ (M = Ti–Cu) bonds stretch. Only the $Sc_{2\text{-}1}$–$Sc_{2\text{-}2}$ distance was reduced slightly.

Table 1
Distances (in Å) between metal and surface atoms and binding energies (in eV) of M_2 in $D(M_2)$ (M = Sc–Cu).

	$M_{2\text{-}1}$–$O_{2c\text{-}1}$	$M_{2\text{-}1}$–$O_{2c\text{-}2}$	$M_{2\text{-}1}$–$Al_{4c\text{-}2}$	$M_{2\text{-}2}$–$O_{3c\text{-}1}$	$M_{2\text{-}2}$–$O_{3c\text{-}2}$	$M_{2\text{-}2}$–$Al_{4c\text{-}2}$	$M_{2\text{-}1}$–$M_{2\text{-}2}$	$\Delta E_{binding}$
$D(Sc_2)$	2.00	2.01	2.70	2.11	2.06	2.76	2.48	4.65
$D(Ti_2)$	1.95	1.96	2.59	2.20	2.34	2.62	2.44	4.19
$D(V_2)$	1.95	2.03	2.62	2.44	3.03	2.83	1.91	3.57
$D(Cr_2)$	1.97	1.97	2.52	2.09	2.07	2.58	1.74	2.07
$D(Mn_2)$	1.97	1.99	2.57	2.04	2.95	2.94	2.51	3.02
$D(Fe_2)$	1.95	2.02	2.52	2.12	3.07	2.94	2.18	3.19
$D(Co_2)$	1.95	2.07	2.42	2.16	3.32	3.26	2.14	3.24
$D(Ni_2)$	1.91	2.09	2.48	2.05	3.23	3.22	2.21	3.24
$D(Cu_2)$	1.99	2.01	2.46	2.08	3.22	3.23	2.29	3.33

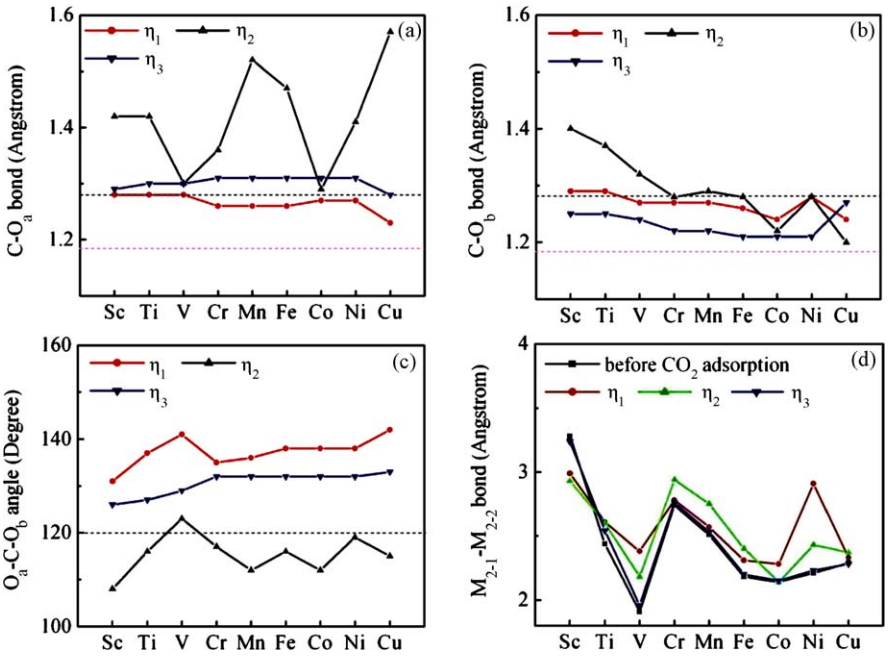

Fig. 3. Variation of C–O_a (a) and C–O_b (b) bond distances, O_a–C–O_b angle (c) and M_{2-1}–M_{2-2} distance (d) in the CO_2 adsorption configurations formed on D(M_2) as M varies from Sc to Cu. The pink dotted lines show the C–O bond distance in free CO_2 molecule. The grey dotted lines denote the C–O bond distance and O–C–O angle in free CO_3^{2-} ion. (For interpretation of the references to color in this figure legend, the reader is referred to the web version of the article.)

The schematic structural model for CO_2 adsorption in η_2 configuration is shown in Fig. 2b. In η_2, CO_2 was adsorbed at the interface between M_2 and the dry surface. The carbon atom interacts with the metal atoms of the dimer. The O_a atom binds the surface Al_{3c} atom whereas the O_b atom shares one of the metal atoms in M_2. The adsorbed CO_2 in η_2 configuration was also distorted from the free CO_2 molecule. Both the C–O_a and C–O_b bonds were elongated, and the C–O_a bond that interacts with both M_2 and the dry surface was further stretched. The variation of the C–O_a bond distance in η_2 configuration as M_2 varies from Sc_2 to Cu_2 was plotted in Fig. 3a. The variation from the left to the right of the periodic table forms a W-shaped curve. The elongation of the C–O_a bond for CO_2 adsorption on D(Sc_2), D(Mn_2), D(Fe_2) and D(Cu_2) is more significant than those on other D(M_2). The most significant elongation of the C–O_a bond occurs on D(Cu_2) where the C–O_a bond was stretched to 1.57 Å. The C–O_b bond, which only interacts with M_2 part of the system, was less stretched than that of the C–O_a bond. In η_2 configuration, the adsorbed CO_2 is also in a bent configuration with the O_a–C–O_b angle of about 108–123° (Fig. 3c). The adsorption of CO_2 in η_2 configuration also caused the M_{2-1}–M_{2-2} (M = Ti to Fe, Ni and Cu) bond to elongate but the Sc_{2-1}–Sc_{2-2} bond to shorten (Fig. 3d). We note that the Co_{2-1}–Co_{2-2} distance was almost the same before and after CO_2 adsorption in this configuration.

The schematic structural model for η_3 configuration is presented in Fig. 2c. In η_3, CO_2 was adsorbed across an O_{2c-3}–Al_{4c-3} bridge site away from the metal dimer as a bidentate carbonate species. The O_a atom was bound to the Al_{4c-3} atom whereas the carbon atom was on the O_{2c-3} atom. The adsorbed CO_2 in η_3 configuration was also distorted from the free CO_2 molecule. In this configuration, the surface is the key factor that induces the distortion of CO_2. The supported metal dimer has an indirect, secondary effect on CO_2 adsorption and activation through the supporting oxide. As shown in Fig. 3d, the changes in the M_{2-1}–M_{2-2} bond distance caused by CO_2 adsorption in η_3 configuration was insignificant as compared with that in bare D(M_2).

The adsorption energies for CO_2 adsorption on D(M_2) are summarized in Table 2. The stability of different adsorption configurations follows the order of $\eta_2 > \eta_1 > \eta_3$. As such, on D(M_2), the most favorable adsorption configuration of CO_2 is η_2 in which CO_2 interacts with both M_2 and the support surface directly. The distortion of the adsorbed CO_2 from the free CO_2 molecule in η_2 configuration is more significant than those in either η_1 or η_3. In Fig. 4, the variation of adsorption energies of CO_2 in different configurations formed on D(M_2) are plotted against the metals. We also showed the variation of the ionization energies of M_2 as M_2 changes from Sc_2 to Cu_2 in Fig. 4. Ionization energy, which is defined as the energy needed to remove an electron from the neutral M_2, has been used to measure the electron-donating ability of M_2 [45–52]. Higher ionization energy generally corresponds to lower electron-donating ability. The ionization energy of the dimer increases from Sc_2 to Cu_2, indicating a decreasing electron-donating ability from left to right across the periodic table. Consequently, CO_2 adsorption energy decreases from the left to the right of the periodic table.

Bader charge analyses were carried out for all adsorption systems. The results are summarized in Table 2. As a reference, the Bader charges for the bare D(M_2) without adsorbed CO_2 are also included in Table 2. Upon CO_2 adsorption, the electronic charges were redistributed among the constituent atoms: (i) the adsorbed CO_2 became negatively charged; (ii) the surface became less negative whereas the supported M_2 became more positive. These results indicated that there was a charge transfer to the adsorbed CO_2 from both M_2 and the surface. The electron transfer from the substrate, including metal and the oxide support, to adsorbed CO_2 resulted in the activation of CO_2, as indicated by the stretched C–O distances in adsorbed CO_2 [18,19,21,53–57]. Our results also showed that the electronic charges on adsorbed CO_2 in η_2 configuration are greater than those in either η_1 or η_3 configuration. For example, on D(Ni_2), the electronic charges on adsorbed CO_2 in η_1, η_2 and η_3 are $-0.61|e|$, $-1.13|e|$ and $-0.43|e|$, respectively. As such, the adsorbed CO_2 in η_2 configuration gained more electronic charge from the substrate and is expected to be more activated than in other configurations. This is consistent with the further stretched C–O_a bond in η_2 configuration, as shown in Fig. 3.

Table 2
Bader charges (in $|e|$) for bare $D(M_2)$ and different CO_2 adsorption configurations on $D(M_2)$ (M = Sc–Cu) as well as the adsorption energies (in eV) of CO_2 in different adsorption configurations. The Bader charges are the sum of the atomic Bader charges of the respective subset of atoms.

	Bader charges			Adsorption energy (ΔE_{ad})
	Dry surface	M_2	Adsorbed CO_2	
$D(Sc_2)$				
Bare	−1.82	1.82		
η_1	−1.60	2.67	−1.07	3.61
η_2	−0.66	2.62	−1.96	4.08
η_3	−1.48	1.97	−0.49	0.54
$D(Ti_2)$				
Bare	−1.37	1.37		
η_1	−1.22	2.10	−0.88	3.46
η_2	−0.36	2.06	−1.70	4.01
η_3	−1.07	1.54	−0.47	0.56
$D(V_2)$				
Bare	−0.93	0.93		
η_1	−1.01	1.75	−0.74	1.70
η_2	−0.45	1.56	−1.11	2.73
η_3	−0.64	1.08	−0.44	0.42
$D(Cr_2)$				
Bare	−1.11	1.11		
η_1	−0.87	1.66	−0.79	1.64
η_2	−0.25	1.60	−1.35	2.93
η_3	−0.73	1.19	−0.46	0.35
$D(Mn_2)$				
Bare	−0.89	0.89		
η_1	−0.71	1.47	−0.76	1.64
η_2	−0.06	1.59	−1.53	3.52
η_3	−0.50	0.95	−0.45	0.34
$D(Fe_2)$				
Bare	−0.64	0.64		
η_1	−0.54	1.20	−0.66	1.30
η_2	0.05	1.33	−1.38	2.89
η_3	−0.26	0.70	−0.44	0.37
$D(Co_2)$				
Bare	−0.47	0.47		
η_1	−0.38	0.97	−0.59	2.00
η_2	−0.12	0.89	−0.77	2.91
η_3	−0.08	0.51	−0.43	0.30
$D(Ni_2)$				
Bare	−0.37	0.37		
η_1	−0.20	0.81	−0.61	0.92
η_2	0.24	0.89	−1.13	3.07
η_3	0.02	0.41	−0.43	0.32
$D(Cu_2)$				
Bare	−0.36	0.36		
η_1	−0.31	0.78	−0.47	0.66
η_2	0.21	0.97	−1.18	2.52
η_3	0.10	0.36	−0.46	0.44

3.3. M_2 supported on the hydroxylated γ-Al_2O_3 (1 1 0) surface

Following the study of CO_2 adsorption over $D(M_2)$, we used the hydroxylated γ-Al_2O_3(1 1 0) surface to characterize the effect of co-adsorbed hydroxyls on CO_2 interaction with the supported metal dimers. The hydroxylated γ-Al_2O_3 (1 1 0) surface for supporting M_2 was established in our previous work [33]. As shown in Fig. 5a, on the hydroxylated surface, the proton and hydroxyl group were bound to the surface $O_{2c\text{-}3}$ and Al_{3c} atoms, respectively, resulting in two OH groups in the unit cell. Again we explored a number of surface sites for M_2 on the hydroxylated surface. The most stable configuration among the configurations for each dimer, denoted as $H(M_2)$, was selected as the substrate for CO_2 adsorption. For example, $H(Ni_2)$ represents the most stable configuration for Ni_2 supported on the hydroxylated γ-Al_2O_3 (1 1 0) surface. A schematic structural model of $H(M_2)$ is shown in Fig. 5b. The location of the metal dimer in $H(M_2)$ is similar to that in $D(M_2)$. The binding energies of M_2 in $H(M_2)$ together with the distances between metal and surface atoms are summarized in Table 3.

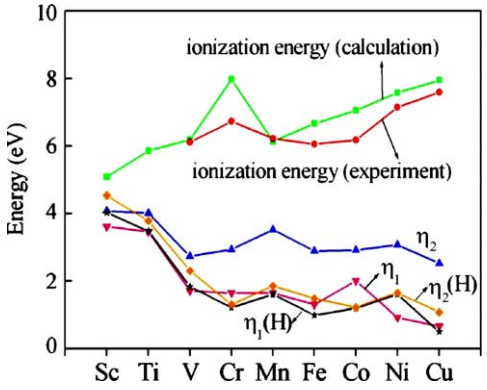

Fig. 4. Variation of adsorption energy of CO_2 in η_1, η_2, η_1(H) and η_2(H) configurations as the function of metal. The calculated and experimentally measured ionization energies of M_2 as the function of metals were also shown. The ionization energies were taken from Refs. [45–52].

As shown in Table 3, Sc_2, with a binding energy of 3.09 eV, shows the strongest binding with the surface among all M_2. The dimer was adsorbed on the surface through the $Sc_{2\text{-}1}$–$O_{2c\text{-}1}$ (2.08 Å), $Sc_{2\text{-}1}$–$O_{2c\text{-}2}$ (2.10 Å), $Sc_{2\text{-}2}$–$O_{3c\text{-}1}$ (2.20 Å) and $Sc_{2\text{-}2}$–$O_{3c\text{-}2}$ (2.11 Å) bonds. The binding energy of Ti_2 in $H(Ti_2)$ is 2.94 eV. $Ti_{2\text{-}1}$–$O_{2c\text{-}1}$ (2.11 Å) and $Ti_{2\text{-}1}$–$O_{2c\text{-}2}$ (2.11 Å) bonds were formed between Ti_2 and the hydroxylated surface. The binding energy of V_2 in $H(V_2)$ is 2.10 eV. In $H(V_2)$, the dimer binds the surface only through the

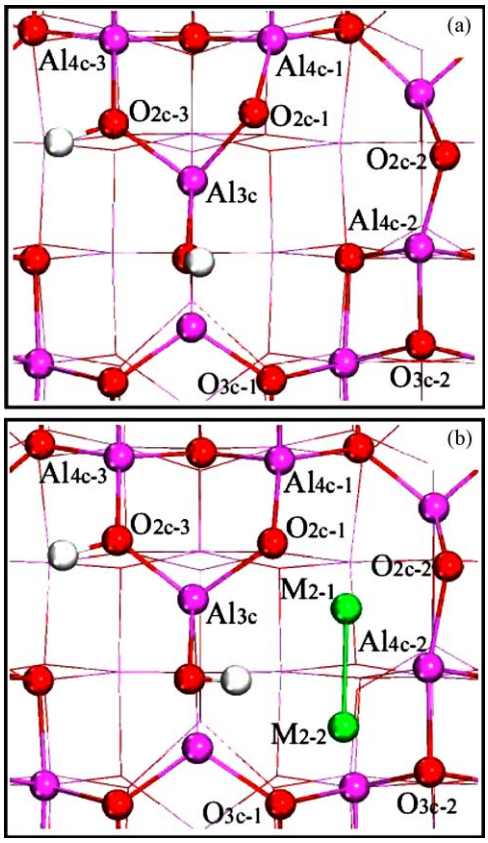

Fig. 5. Top view of the hydroxylated γ-Al_2O_3 (1 1 0) surface (a) and schematic structural model of $H(M_2)$ (b). Color coding: white, H atoms; others are the same as in Fig. 1.

Table 3
Distances (in Å) between metal and surface atoms and binding energies (in eV) of M_2 in H(M_2) (M = Sc–Cu).

	$M_{2\text{-}1}$–$O_{2c\text{-}1}$	$M_{2\text{-}1}$–$O_{2c\text{-}2}$	$M_{2\text{-}1}$–$Al_{4c\text{-}2}$	$M_{2\text{-}2}$–$O_{3c\text{-}1}$	$M_{2\text{-}2}$–$O_{3c\text{-}2}$	$M_{2\text{-}2}$–$Al_{4c\text{-}2}$	$M_{2\text{-}1}$–$M_{2\text{-}2}$	$\Delta E_{binding}$
H(Sc_2)	2.08	2.10	2.69	2.20	2.11	2.68	2.33	3.09
H(Ti_2)	2.11	2.11	2.57	2.36	2.33	2.55	2.27	2.94
H(V_2)	2.10	2.09	2.68	3.86	3.46	2.79	1.80	2.10
H(Cr_2)	2.16	2.13	2.68	3.98	3.46	2.82	1.64	1.73
H(Mn_2)	2.18	2.30	2.52	2.48	2.18	2.52	2.47	2.03
H(Fe_2)	2.12	2.63	2.52	2.38	2.24	2.51	2.14	2.36
H(Co_2)	2.01	2.09	2.47	3.63	2.98	2.56	2.06	2.39
H(Ni_2)	2.02	2.60	2.48	2.44	2.08	2.37	2.20	2.44
H(Cu_2)	1.98	2.56	2.59	3.18	2.36	2.40	2.28	2.92

$V_{2\text{-}1}$ atom, with the $V_{2\text{-}1}$–$O_{2c\text{-}1}$ and $V_{2\text{-}1}$–$O_{2c\text{-}2}$ distances of 2.10 Å and 2.09 Å, respectively. The $V_{2\text{-}2}$ atom does not interact with the surface atoms directly. The binding energy of Cr_2 in H(Cr_2) is lower by 0.37 eV than that of V_2 in H(V_2). Cr_2 interacts with the surface through $Cr_{2\text{-}1}$–$O_{2c\text{-}1}$ (2.16 Å) and $Cr_{2\text{-}1}$–$O_{2c\text{-}2}$ (2.13 Å) bonds. From Cr_2 to Cu_2, the binding energy increases slightly. The binding energy of Mn_2, Fe_2, Co_2, Ni_2 and Cu_2 in H(Mn_2), H(Fe_2), H(Co_2), H(Ni_2) and H(Cu_2) are 2.03 eV, 2.36 eV, 2.39 eV, 2.44 eV and 2.92 eV, respectively. H(Mn_2), H(Fe_2), H(Ni_2) and H(Cu_2) have a similar structure: the dimer binds the surface through both ends: $M_{2\text{-}1}$–$O_{2c\text{-}1}$ and $M_{2\text{-}2}$–$O_{3c\text{-}2}$. For instance, $Mn_{2\text{-}1}$–$O_{2c\text{-}1}$ and $Mn_{2\text{-}2}$–$O_{3c\text{-}2}$ in H(Mn_2) are both 2.18 Å. In H(Co_2), the $Co_{2\text{-}1}$–$O_{2c\text{-}1}$ and $Co_{2\text{-}1}$–$O_{2c\text{-}2}$ are 2.01 Å and 2.09 Å, respectively.

3.4. CO_2 adsorption and activation on H(M_2)

In Section 3.2, we showed that CO_2 can be adsorbed across the surface $O_{2c\text{-}3}$-$Al_{4c\text{-}3}$ bridge site to form adsorption configuration η_3 on D(M_2). We also showed that the $O_{2c\text{-}3}$ and Al_{3c} sites may be occupied by hydroxyls [33]. Consequently, hydroxylation of the surface is expected to drive CO_2 adsorption to the supported metal dimer, either interacting with the dimer only or at the interface of the dimer and the support. We examined CO_2 adsorption on H(M_2) and focus our attention on the sites in the vicinity of the metal dimer. Among configurations on H(M_2) that were explored for CO_2 adsorption, two were found to be stable. The first one has a local structure that is similar to η_1 on D(M_2) and is denoted as η_1(H), whereas the second one has a similar local structure to that of η_2 on D(M_2) and is referred to as η_2(H).

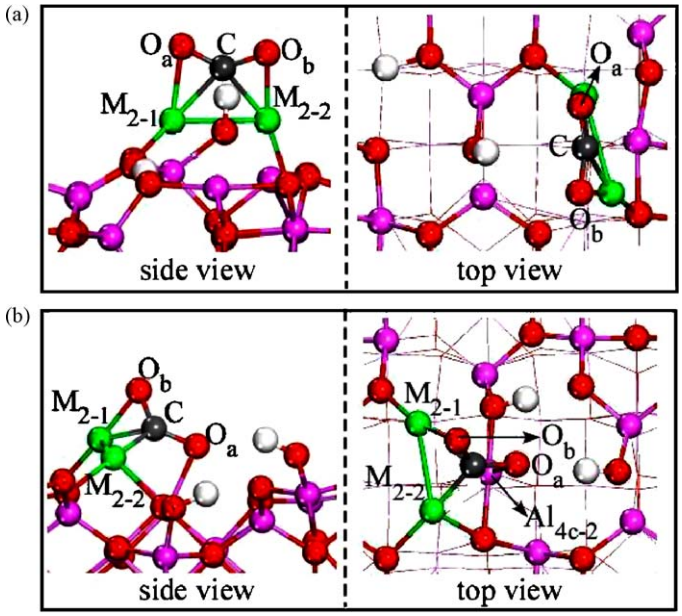

Fig. 6. Schematic structural models of η_1(H) (a) and η_2(H) (b) configurations. See Figs. 1, 2 and 5 for color coding.

A schematic structural model of η_1(H) is shown in Fig. 6a. In η_1(H), the carbon atom interacts with both metal atoms whereas the O_a and O_b atoms bind the $M_{2\text{-}1}$ and $M_{2\text{-}2}$ atoms, respectively. The distortion of adsorbed CO_2 from the free CO_2 molecule is again summarized in a plot, shown in Fig. 7, where the variation of the C–O_a and C–O_b distances and the O_a–C–O_b angle are plotted as a function of metals. Similar to CO_2 adsorption on D(M_2), both C–O_a and C–O_b bonds were stretched and the O_a–C–O_b angle was reduced in η_1(H) configuration (Fig. 7a–c). For instance, in η_1(H) formed upon CO_2 adsorption on H(Ni_2), the C–O_a and C–O_b bonds were stretched to 1.24 Å and 1.30 Å, respectively, and the O_a–C–O_b angle was reduced to 130°. As shown in Fig. 7d, adsorption of CO_2 in η_1(H) configuration makes the $M_{2\text{-}1}$–$M_{2\text{-}2}$ distance in supported M_2 with M = Ti to Cu longer whereas the $Sc_{2\text{-}1}$–$Sc_{2\text{-}2}$ distance is shorter than the corresponding $M_{2\text{-}1}$–$M_{2\text{-}2}$ distance prior to CO_2 adsorption.

Fig. 6b shows the schematic structural model of η_2(H) configuration. In η_2(H), CO_2 interacts with both the dimer and the surface. The carbon atom binds both metal atoms in M_2 whereas the O_a and O_b atoms interact with the surface $Al_{4c\text{-}2}$ atom and one of the metal atoms in M_2, respectively. The adsorbed CO_2 in η_2(H) configuration was also distorted from the free CO_2 molecule, moreover, the distortion of CO_2 in η_2(H) is more significant than that in η_1(H) (Fig. 7a–c). Compared with the bare H(M_2), adsorption of CO_2 in η_2(H) configuration caused the $M_{2\text{-}1}$–$M_{2\text{-}2}$ (M = Sc, Ti, Cr–Cu) distance to elongate and the $V_{2\text{-}1}$–$V_{2\text{-}2}$ bond to shorten, as shown in Fig. 7d.

The adsorption energies for CO_2 on H(M_2) are summarized in Table 4. The stability of η_2(H) configuration is higher than that of η_1(H) configuration. This again indicates that the interface between M_2 and the surface is more favorable for CO_2 adsorption on H(M_2). We plotted the adsorption energies of CO_2 in η_1(H) and η_2(H) configurations as a function of metals in Fig. 4. As shown in Fig. 4, the strength of the interaction between CO_2 and H(M_2) becomes weaker as M_2 changes from Sc_2 to Cu_2.

Bader charges were calculated for all adsorption configurations formed upon CO_2 adsorption on H(M_2) and are summarized in Table 4. The Bader charges for the bare H(M_2) are also given as references. Again, a charge transfer from both the dimer and the support to the adsorbed CO_2 occurred. The charge accumulation in adsorbed CO_2 resulted in activation of CO_2. Furthermore, the charges on the adsorbed CO_2 in η_2(H) configuration are greater than that in η_1(H) configuration for the same metal, indicating that the adsorbed CO_2 gained more electrons from the substrate in η_2(H) configuration. The greater electronic transfer led to a more pronounced distortion of CO_2 in η_2(H) configuration.

3.5. General discussion

As we noted in previous sections, M_2 was adsorbed at a position that is surrounded by O_{2c}, O_{3c}, Al_{3c} and Al_{4c} atoms on both the dry

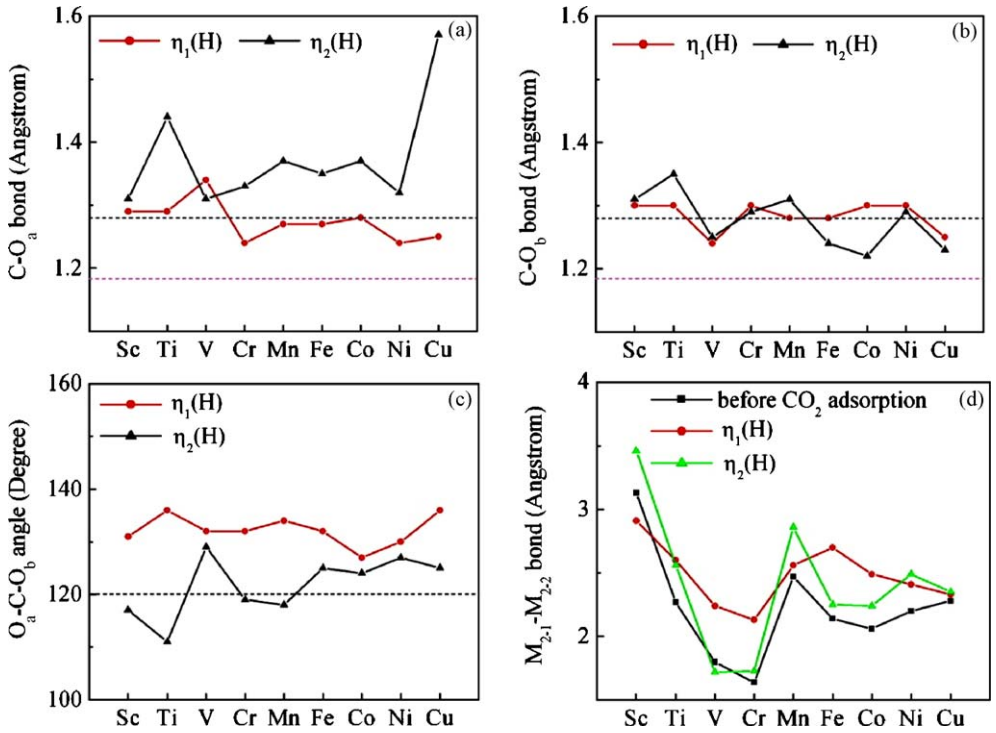

Fig. 7. Variation of C–O_a (a) and C–O_b (b) bond distances, O_a–C–O_b angle (c) and $M_{2\text{-}1}$–$M_{2\text{-}2}$ distance (d) in different adsorption configurations formed on H(M_2) as a function of metals. The pink and grey dotted lines are for free CO_2 and CO_3^{2-}, as shown in Fig. 3. (For interpretation of the references to color in this figure legend, the reader is referred to the web version of the article.)

and hydroxylated γ-Al_2O_3 (1 1 0) surfaces. Furthermore, the binding energy of the dimer on the dry surface varies in a similar trend to that on the hydroxylated surface: the binding energy first decreases from Sc_2 to Cr_2, and then increases slowly from Cr_2 to Cu_2. As shown in Tables 1 and 3, the binding energy of M_2 in D(M_2) is greater than that in H(M_2), indicating that hydroxylation of the surface weakens the binding of M_2 to the surface.

As shown in Fig. 1a, there are two O_{2c}–Al_{3c} ($O_{2c\text{-}1}$–Al_{3c} and $O_{2c\text{-}3}$–Al_{3c}) and three O_{2c}–Al_{4c} ($O_{2c\text{-}1}$–$Al_{4c\text{-}1}$, $O_{2c\text{-}2}$–$Al_{4c\text{-}2}$ and $O_{2c\text{-}3}$–$Al_{4c\text{-}3}$) sites on the clean dry γ-Al_2O_3 (1 1 0) surface. In our previous work [33], we demonstrated that the O_{2c}–Al_{3c} ($O_{2c\text{-}1}$–Al_{3c} or $O_{2c\text{-}3}$–Al_{3c}) bridge site is the most favorable site for CO_2 adsorption on the clean dry surface. CO_2 can also be adsorbed at the O_{2c}–Al_{4c} ($O_{2c\text{-}1}$–$Al_{4c\text{-}1}$, $O_{2c\text{-}2}$–$Al_{4c\text{-}2}$ or $O_{2c\text{-}3}$–$Al_{4c\text{-}3}$) bridge site, but the binding strength of CO_2 at the O_{2c}–Al_{4c} site is weaker than that at the O_{2c}–Al_{3c} site. The adsorption energies for CO_2 adsorption at the O_{2c}–Al_{3c} and O_{2c}–Al_{4c} bridge sites of the clean dry surface were 0.43 eV and 0.27 eV, respectively. On the hydroxylated γ-Al_2O_3 (1 1 0) surface, the $O_{2c\text{-}3}$ and Al_{3c} sites were occupied by hydroxyls (Fig. 5a). Due to the occupation of the $O_{2c\text{-}3}$ and Al_{3c} sites by hydroxyls, the O_{2c}–Al_{4c} ($O_{2c\text{-}1}$–$Al_{4c\text{-}1}$ or $O_{2c\text{-}2}$–$Al_{4c\text{-}2}$) bridge site became favorable for CO_2 adsorption on the hydroxylated surface. The adsorption energy for CO_2 adsorption at the O_{2c}–Al_{4c} bridge site of the hydroxylated surface was 0.20 eV [33].

Among three CO_2 adsorption configurations, η_1, η_2 and η_3, the adsorption energies of CO_2 in η_1 and η_2 are clearly much higher than that of CO_2 on the dry surface [33]. Even in η_3 configuration where CO_2 was adsorbed at a surface O_{2c}–Al_{4c} bridge site, the adsorption energy on D(M_2) is greater than that of CO_2 adsorption at the O_{2c}–Al_{4c} site of the clean dry surface. Two adsorption configurations examined on H(M_2), η_1(H) and η_2(H), are similar to η_1 and η_2, respectively. The adsorption energies for CO_2 in η_1(H) and η_2(H) are also much greater than that of CO_2 on the hydroxylated surface. As such, the interaction between CO_2 and H(M_2) is much stronger than that of CO_2 with the hydroxylated surface. These results illustrated that the presence of M_2 enhances the binding strength of the substrate toward CO_2.

Following Ref. [24], the adsorption of CO_2 on M_2/γ-Al_2O_3 can be considered as a two-step process: first, CO_2 deforms from its linear gas phase structure into a bent CO_2 fragment; second, the bent CO_2 fragment binds M_2/γ-Al_2O_3. The process is shown schematically in Fig. 8. We defined the energy cost for the first step as distortion energy and the energy gain for the second step as binding energy. The sum of the energies of these two steps yields the adsorption energy. In Fig. 9a, we plot the distortion energy of CO_2 in η_2 and η_2(H) against the electronic charges on adsorbed CO_2. As shown in the plot, there is approximately a linear relationship between the distortion energy and the electronic charges in both η_2 and η_2(H) configurations. Furthermore, the two lines describing the linear relationship in η_2 and η_2(H) configurations are almost coincident. The variation of the binding energies as a function of the electronic charges on adsorbed CO_2 in η_2 and η_2(H) configurations is plotted in Fig. 9b. Again, linear correlation between the binding energy and the charges on the adsorbed CO_2 in both η_2 and η_2(H) configurations exists. However, we note that the slope of binding energy for η_2(H) configuration is greater than that for η_2 configuration. This can be attributed to a greater change in electron-donating ability for the early transition metal than for the late ones due to hydroxylation. Generally, hydroxylation reduced the amount of charge transferred to CO_2, as shown in Fig. 9. Consequently, hydroxylation compresses the range of charge transfer across the periodic table. We note, however, hydroxylation increases the electronic charges on adsorbed CO_2 in η_2(H) configuration for Co_2/γ-Al_2O_3.

Improving the adsorption and activation of CO_2 on the catalysts is expected to benefit the conversion of CO_2, and therefore, the activity and selectivity. Our present results showed that the interface between the metal dimer and the γ-Al_2O_3 support is the most favorable site for CO_2 adsorption and CO_2 becomes activated upon adsorption at this site. This can be achieved in practice by increasing the dispersion of metal on the support. For the same

Table 4
Bader charges (in $|e|$) for bare $H(M_2)$ and different CO_2 adsorption configurations on $H(M_2)$ (M = Sc–Cu) as well as the adsorption energies (in eV) of CO_2 in different adsorption configurations. The Bader charges are the sum of the atomic Bader charges of the respective subset of atoms.

	Bader charges			Adsorption energy (ΔE_{ad})
	Hydroxylated surface	M_2	Adsorbed CO_2	
$H(Sc_2)$				
Bare	−1.54	1.54		
$\eta_1(H)$	−1.29	2.45	−1.16	4.03
$\eta_2(H)$	−0.97	2.32	−1.35	4.53
$H(Ti_2)$				
Bare	−1.02	1.02		
$\eta_1(H)$	−0.94	1.90	−0.96	3.48
$\eta_2(H)$	−0.38	1.93	−1.55	3.79
$H(V_2)$				
Bare	−0.55	0.55		
$\eta_1(H)$	−0.64	1.50	−0.86	1.83
$\eta_2(H)$	−0.16	1.20	−1.04	2.30
$H(Cr_2)$				
Bare	−0.50	0.50		
$\eta_1(H)$	−0.38	1.25	−0.87	1.21
$\eta_2(H)$	−0.05	1.22	−1.17	1.23
$H(Mn_2)$				
Bare	−0.75	0.75		
$\eta_1(H)$	−0.49	1.37	−0.88	1.60
$\eta_2(H)$	−0.19	1.52	−1.33	1.86
$H(Fe_2)$				
Bare	−0.54	0.54		
$\eta_1(H)$	−0.36	1.19	−0.83	0.99
$\eta_2(H)$	0.08	1.11	−1.03	1.48
$H(Co_2)$				
Bare	−0.35	0.35		
$\eta_1(H)$	−0.15	0.96	−0.81	1.20
$\eta_2(H)$	−0.04	0.94	−0.98	1.22
$H(Ni_2)$				
Bare	−0.31	0.31		
$\eta_1(H)$	−0.09	0.70	−0.61	1.60
$\eta_2(H)$	0.11	0.86	−0.97	1.64
$H(Cu_2)$				
Bare	−0.25	0.25		
$\eta_1(H)$	−0.14	0.71	−0.57	0.50
$\eta_2(H)$	0.06	0.87	−0.93	1.09

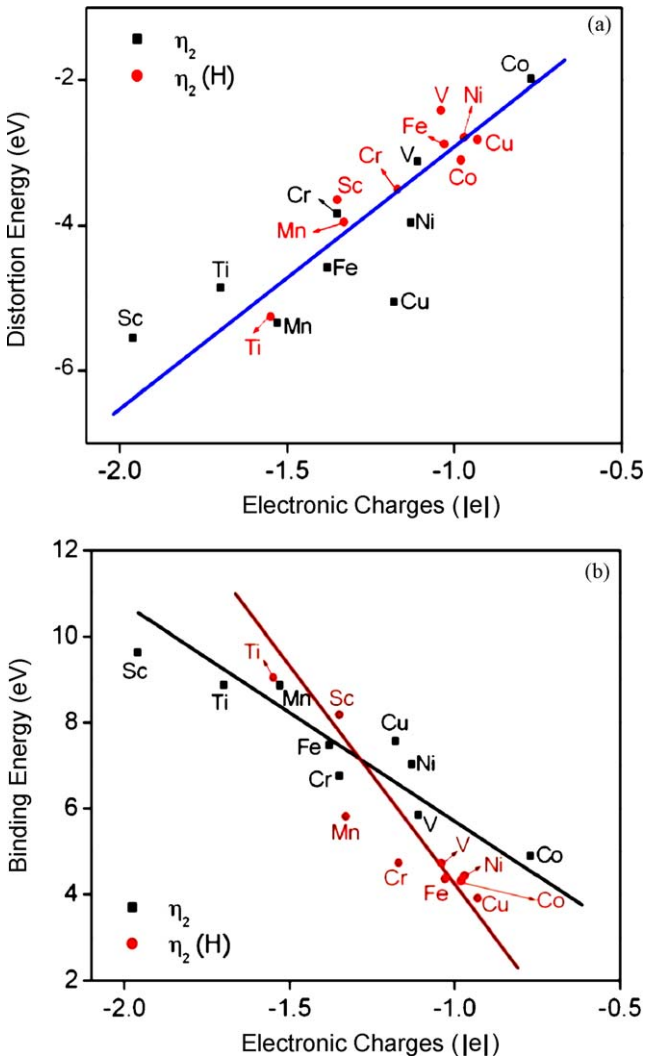

Fig. 9. Variation of the distortion energy (a) and binding energy (b) of CO_2 in η_2 and $\eta_2(H)$ configurations as a function of the electronic charges on adsorbed CO_2.

metal loading, a large particle will lead to a reduced interface, therefore, low activity. Increasing the dispersion of the metal particles and maintaining the smaller size of supported metal particles will maximize the interface available for CO_2 adsorption. Furthermore, CO_2 adsorbed at the interface is more activated, manifested by the stretched C–O bond. The activated CO_2 will make the subsequent reaction facile. These analyses are consistent with the experimental observation that the catalysts with smaller metal particles and higher particle dispersion show a high activity in the catalytic conversion of CO_2.

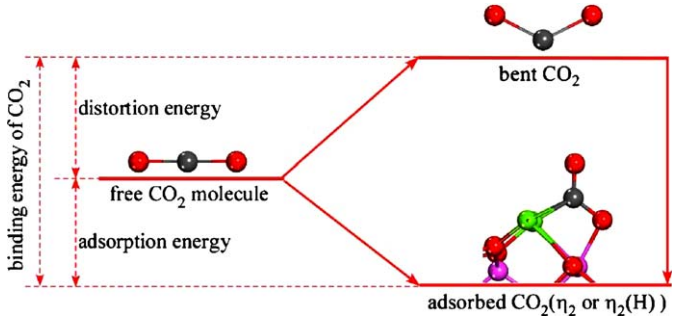

Fig. 8. Schematic of distortion and binding steps of CO_2.

4. Conclusions

The adsorption and activation of CO_2 on γ-Al_2O_3-supported 3d transition metal dimers (M_2/γ-Al_2O_3, M = Sc–Cu) have been studied using DFT slab calculations. CO_2 was found to adsorb on M_2/γ-Al_2O_3 negatively charged and in bent configuration, indicating a partial activation of CO_2. Both the supported metal dimer and the support, either dry or partially hydroxylated γ-Al_2O_3, contribute to the activation of CO_2 by donating their electronic charges to the adsorbed CO_2. The most favorable adsorption site for CO_2 on M_2/γ-Al_2O_3, either dry or partially hydroxylated support, is the interface between the metal dimer and the support. The electronic charges on the adsorbed CO_2 make CO_2 distort from its linear configuration in the gas phase. The presence of the metal dimer enhances the binding of CO_2 with the substrate, including both dry and partially hydroxylated γ-Al_2O_3. As such, the adsorption energy of CO_2 on M_2/γ-Al_2O_3 is much higher than that on the γ-Al_2O_3 surfaces without supported metal dimer. We also demonstrated that the binding strength of CO_2 with M_2/γ-Al_2O_3 correlates with the electron-donating ability of the substrate. Both distortion energy and CO_2 binding energy show

a linear dependence on the amount of charge on the adsorbed CO_2. The 3d metal on the left of the periodic table has a greater electron-donating ability which resulted in a stronger CO_2 binding. Hydroxylation of the support surface reduces the amount of charge transferred to CO_2 for the same metal dimer and weakens the CO_2 chemisorption bonds. Highly dispersed metal particles maintained at a small size are expected to exhibit good activity toward CO_2 adsorption and activation.

Acknowledgements

We gratefully acknowledge support from the Petroleum Research Fund (PRF-G44103-G10), the National Natural Science Foundation of China (under contract 20490203), and the Illinois Clean Coal Institute.

References

[1] A.T. Bell, B.C. Gates, D. Ray, Basic Research Needs: Catalysis for Energy, US DOE, 2007 http://www.sc.doe.gov/bes/reports/files/CAT_rpt.pdf.
[2] E. Ruckenstein, H.Y. Wang, J. Catal. 205 (2002) 289.
[3] C.S. Song, Catal. Today 115 (2006) 2.
[4] Y.H. Hu, E. Ruckenstein, Adv. Catal. 48 (2004) 297.
[5] Y.X. Pan, C.J. Liu, L. Cui, Catal. Lett. 123 (2008) 96.
[6] Y.X. Pan, C.J. Liu, P. Shi, J. Power Sources 176 (2008) 46.
[7] X.L. Zhu, P.P. Huo, Y.P. Zhang, D.G. Cheng, C.J. Liu, Appl. Catal. B. 81 (2008) 132.
[8] E. Ruckenstein, Y.H. Hu, J. Catal. 162 (1996) 230.
[9] J.R. Rostrup-Nielsen, J.H.B. Hansen, J. Catal. 144 (1993) 38.
[10] T. Osaki, T. Mori, J. Catal. 204 (2001) 89.
[11] D.G. Cheng, X.L. Zhu, Y.H. Ben, F. He, L. Cui, C.J. Liu, Catal. Today 115 (2006) 205.
[12] L. Znak, K. Stolecki, J. Zielinski, Catal. Today 101 (2005) 65.
[13] A.E. Aksoylu, A.N. Akin, Z.I. Onsan, D.L. Trimm, Appl. Catal. A: Gen. 145 (1996) 185.
[14] A.E. Aksoylu, Z.I. Önsan, Appl. Catal. A: Gen. 164 (1997) 1.
[15] X. An, J.L. Li, Y.Z. Zuo, Q. Zhang, D.Z. Wang, J.F. Wang, Catal. Lett. 118 (2007) 264.
[16] G.X. Qi, X.M. Zheng, J.H. Fei, Z.Y. Hou, Catal. Lett. 72 (2001) 191.
[17] H.J. Freund, M.W. Roberts, Surf. Sci. Rep. 25 (1996) 225.
[18] E. Vesselli, L. De Rogatis, X.L. Ding, A. Baraldi, L. Savio, L. Vattuone, M. Rocca, P. Fornasiero, M. Peressi, A. Baldereschi, R. Rosei, G. Comelli, J. Am. Chem. Soc. 130 (2008) 11417.
[19] S.G. Wang, D.B. Cao, Y.W. Li, J.G. Wang, H.J. Jiao, J. Phys. Chem. B 109 (2005) 18956.
[20] G. Meyer, D. Borgmann, G. Wedler, Surf. Sci. 320 (1994) 123.
[21] G. Meyer, E. Reinhart, D. Borgmann, G. Wedler, Surf. Sci. 320 (1994) 110.
[22] C. de Leitenburg, A. Trovarelli, J. Kaspar, J. Catal. 166 (1997) 98.
[23] M.A. Henderson, S.D. Worley, J. Phys. Chem. 89 (1985) 392.
[24] M.C. Valero, P. Raybaud, P. Sautet, J. Catal. 247 (2007) 339.
[25] M.Y. Sun, A.E. Nelson, J. Adjaye, J. Phys. Chem. B 110 (2006) 2310.
[26] M. Digne, P. Raybaud, P. Sautet, B. Rebours, H. Toulhoat, J. Phys. Chem. B 110 (2006) 20719.
[27] M. Digne, P. Sautet, P. Raybaud, P. Euzen, H. Toulhoat, J. Catal. 226 (2004) 54.
[28] G. Paglia, A.L. Rohl, C.E. Buckley, J.D. Gale, Phys. Rev. B 71 (2005) 224115.
[29] H.P. Pinto, R.M. Nieminen, S.D. Elliott, Phys. Rev. B 70 (2004) 125402.
[30] D. Mei, Q. Ge, J.H. Kwak, D.H. Kim, J. Szanyi, C.H.F. Peden, J. Phys. Chem. C 112 (2008) 18050.
[31] L. Cheng, Q. Ge, Surf. Sci. 601 (2007) L65.
[32] L. Cheng, Q. Ge, J. Phys. Chem. C 112 (2008) 16924.
[33] Y.X. Pan, C.-J. Liu, Q. Ge, Langmuir 24 (2008) 12410.
[34] J.H. Kwak, J.Z. Hu, D.H. Kim, J. Szanyi, C.H.F. Peden, J. Catal. 251 (2007) 189.
[35] J.H. Kwak, J.Z. Hu, A. Lukaski, D.H. Kim, J. Szanyi, C.H.F. Peden, J. Phys. Chem. C 112 (2008) 9486.
[36] P.D. Nellist, S.J. Pennycook, Science 274 (1996) 413.
[37] G. Kresse, J. Hafner, Phys. Rev. B 48 (1993) 13115.
[38] G. Kresse, D. Joubert, Phys. Rev. B 59 (1999) 1758.
[39] P.E. Blochl, Phys. Rev. B 50 (1994) 17953.
[40] J. Liu, Y. Han, Q. Ge, Chem. Eur. J. 15 (2009) 1685.
[41] J.P. Perdew, K. Burke, M. Ernzerhof, Phys. Rev. Lett. 77 (1996) 3865.
[42] H.J. Monkhorst, J.D. Pack, Phys. Rev. B 13 (1976) 5188.
[43] R.F.W. Bader, Accounts Chem. Res. 18 (1985) 9.
[44] G. Henkelman, A. Arnaldsson, H. Jonsson, Comp. Mater. Sci. 36 (2006) 354.
[45] E.A. Rohlfing, D.M. Cox, A. Kaldor, K.H. Johnson, J. Chem. Phys. 81 (1984) 3846.
[46] L. Jiang, Q. Xu, J. Chem. Phys. 128 (2008) 124317.
[47] A.M. James, P. Kowalczyk, E. Langlois, M.D. Campbell, A. Ogawa, B. Simard, J. Chem. Phys. 101 (1994) 4485.
[48] M.F. Jarrold, A.J. Illies, M.T. Bowers, J. Am. Chem. Soc. 107 (1985) 7339.
[49] B. Simard, M.A. Lebeault-Dorget, A. Marijnissen, J.J. ter Meulen, J. Chem. Phys. 108 (1998) 9668.
[50] D.A. Hales, C.X. Su, L. Lian, P.B. Armentrout, J. Chem. Phys. 100 (1994) 1049.
[51] J.C. Pinegar, J.D. Langenberg, C.A. Arrington, E.M. Spain, M.D. Morse, J. Chem. Phys. 102 (1995) 666.
[52] A.D. Sappey, J.E. Harrington, J.C. Weisshaar, J. Chem. Phys. 91 (1989) 3854.
[53] X. Ding, L. De Rogatis, E. Vesselli, A. Baraldi, G. Comelli, R. Rosei, L. Savio, L. Vattuone, M. Rocca, P. Fornasiero, F. Ancilotto, A. Baldereschi, M. Peressi, Phys. Rev. B 76 (2007) 195425.
[54] S.J. Choe, H.J. Kang, D.H. Park, D.S. Huh, J. Park, Appl. Surf. Sci. 181 (2001) 265.
[55] S.G. Wang, D.B. Cao, Y.W. Li, J.G. Wang, H.J. Jiao, J. Phys. Chem. B 110 (2006) 9976.
[56] F. Solymosi, J. Kiss, Surf. Sci. 149 (1985) 17.
[57] H.A.C.M. Hendrickx, A.P.J.M. Jongenelis, B.E. Nieuwenhuys, Surf. Sci. 154 (1985) 503.